

# Journal of Geophysical Research: Atmospheres

## RESEARCH ARTICLE

10.1002/2014JD021855

**Key Points:**

- Future regional climate projections over the Great Lakes Basin
- Both average and extreme rainfall increase by 7% per degree of warming
- Future fattening of the tail of the daily precipitation distribution

**Correspondence to:**

M. d'Orgeville,  
marcdo@atmosphysics.utoronto.ca

**Citation:**

d'Orgeville, M., W. R. Peltier, A. R. Erler, and J. Gula (2014), Climate change impacts on Great Lakes Basin precipitation extremes, *J. Geophys. Res. Atmos.*, 119, doi:10.1002/2014JD021855.

Received 8 APR 2014

Accepted 1 SEP 2014

Accepted article online 23 SEP 2014

## Climate change impacts on Great Lakes Basin precipitation extremes

**Marc d'Orgeville<sup>1,2</sup>, W. Richard Peltier<sup>1</sup>, Andre R. Erler<sup>1</sup>, and Jonathan Gula<sup>3</sup>**

<sup>1</sup>Department of Physics, University of Toronto, Toronto, Ontario, Canada, <sup>2</sup>Canadian Research and Development Centre, IBM, Toronto, Ontario, Canada, <sup>3</sup>Department of Atmospheric and Oceanic Sciences, University of California, Los Angeles, California, USA

**Abstract** A physics-based miniensemble of Weather Research and Forecasting model simulations of climate change over the Great Lakes Basin has been constructed, by dynamically downscaling a single global Community Earth System Model 1 simulation driven by the Representative Concentration Pathways 8.5 scenario. The analysis pipeline is successfully verified by comparison of the results with observations for the historical period (1979–1994) and then applied to produce future projections (2045–2060). By midcentury, in this miniensemble, the future change in rainfall distribution is projected to correspond to an increase of total rainfall (median increase of between 13 and 19%) characterized by a fattening of the tail of the distribution (median increase of between 14 and 29% of the amplitude of a 50 year extreme rainfall event). Average rainfall intensity changes are shown to accurately follow the “Clausius–Clapeyron” thermodynamically expected 7% increase per degree of surface warming, whereas heavy rainfall changes are found to lie between 7 and 10% per degree of surface warming. This further increase can be explained by two effects in the Great Lakes region: midtropospheric warming is projected to be larger than surface warming and heavy rainfall events are projected to originate from higher altitude where additional moisture is available. Details of the physics configuration play only a secondary role in determining the future precipitation changes, primarily through their impact on future temperature changes. The uncertainty in the future projection of precipitation and its extremes therefore depends primarily upon the uncertainty in projected future warming which will require implementation of a larger ensemble of projections to be more accurately assessed.

### 1. Introduction

Because of their significant size, the Great Lakes have a large influence on the climate of their region, primarily due to the pronounced land-water contrasts and to the large source of moisture that they provide. The major effects of the lakes are to reduce the amplitude of both diurnal and annual cycles of air temperatures, to increase cloud cover and precipitation downwind of the lakes during winter, and to diminish convective clouds and rainfall in summer due to a greater atmospheric stability imparted by the cool water [e.g., Notaro *et al.*, 2013, and references herein]. In this context, understanding the potential moderation effect of the Great Lakes on future climate change is scientifically interesting, but with over 35 million inhabitants living within their watershed, it is also a vital question to the economies of both U.S. and Canada.

This study addresses the characteristics of future changes of daily precipitation to be expected over the Great Lakes Basin of North America as a consequence of the climate change process. Past average and extreme precipitation indices for the region increased during the twentieth century [Alexander *et al.*, 2006; Mekis and Vincent, 2011] and are expected to continue to increase during the 21st century as warming continues, according to the results of the two most recent Coupled Model Intercomparison Projects, CMIP3 and CMIP5 [Tebaldi *et al.*, 2006; Kharin *et al.*, 2007, 2013]. However, at the resolution of the global coupled models employed in CMIP3 and CMIP5, the projected future changes are represented solely by extremely large-scale patterns, and moreover, the effect of the Great Lakes themselves on local meteorology are poorly represented if at all [e.g., Gula and Peltier, 2012]. To remedy this deficiency, we are conducting a series of increasingly high-resolution regional downscaling experiments, in order to improve the physical representation of precipitation extremes which have small spatial scale and to properly account for the pronounced land-water contrasts which are expected to add value to results derived on the basis of high-resolution dynamical downscaling [Di Luca *et al.*, 2013].

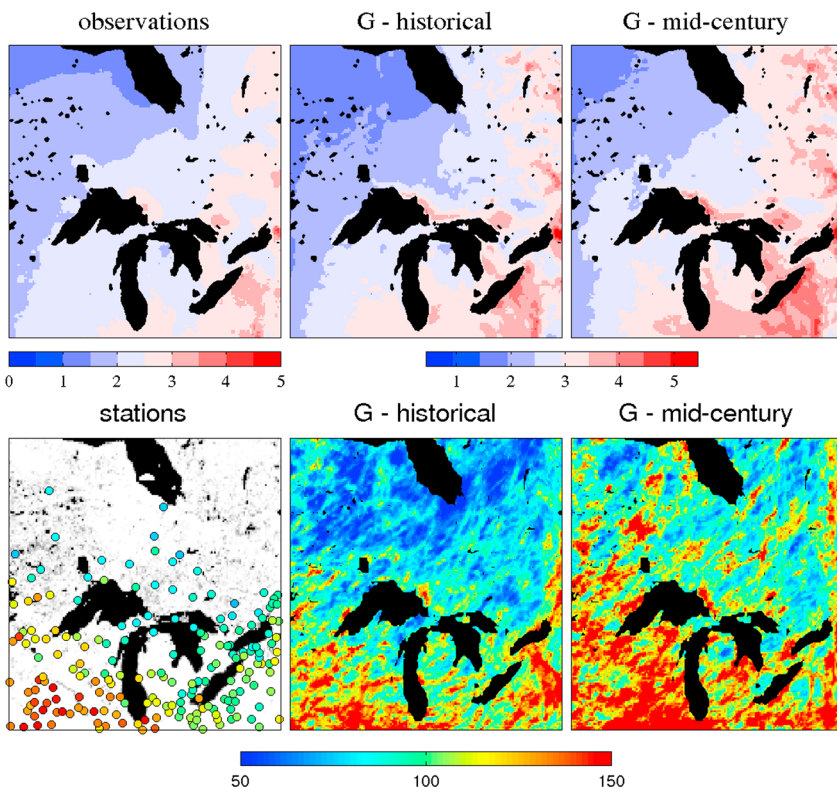


**Figure 1.** (top row) Yearly average of daily precipitation ( $\text{Rain}_{\text{tot}}$ ) and (bottom row) the extreme 50 year return value of daily precipitation distribution ( $X^{50}$ ) for historical observations (left), one historical simulation (center), and one future simulation (right). Both simulations are from configuration G for years 1979–1994 and 2045–2059. Observation for the average are from years 1979–1994 of the CONUS and Natural Resources Canada (NRCan) data sets. Observations for the extreme values are from the extreme value analysis of daily precipitation time series of 193 Canadian and U.S. weather stations (see text for details). Units on all frames are in mm/d.

The projected increase by midcentury of average and extreme precipitation over the Great Lakes region can be seen in Figure 1 on which we compare the results obtained for one historical and one future simulation (center and right panels, respectively). These panels are based upon the Weather Research and Forecasting (WRF) configuration from those in the physics ensemble which best represents the historical observations of precipitation (leftmost panel; both observations and simulations are fully discussed in what follows). Whereas the sign of the future precipitation changes is not in doubt for the Great Lakes region (see Figures 3 and 4 of Tebaldi *et al.* [2006] and Kharin *et al.* [2013], respectively), one purpose of this study is to investigate the utility of the thermodynamical constraint based on the Clausius-Clapeyron relation as a means of understanding not only the increase of mean precipitation but also upon its extremes. The relationship  $\Delta e_s/e_s = LR\Delta T$  (in which  $R$  is the gas constant for water vapor,  $L$  the specific latent heat of evaporation,  $e_s$  the saturation vapor pressure, and  $T$  temperature) implies an approximate exponential variation of moisture availability with temperature change of approximately 7% increase per  $^{\circ}\text{C}$  of warming as is well known.

This value of 7% per  $^{\circ}\text{C}$  has also been suggested to be a good predictor of extreme precipitation changes, in fact an even better predictor than for average changes [Pall *et al.*, 2007]. However, because both average and extreme precipitation changes can also be influenced by circulation changes in midlatitudes [Meehl *et al.*, 2005], the primary explanation for the precipitation changes expected to occur in the Great Lakes region remains uncertain. Following validation of the downscaling pipeline against both average and extreme precipitation in the set of experiments that comprise our physics based miniensemble, the focus of the analyses to follow will be upon an investigation of the extent to which the thermodynamic constraint is able to provide an accurate prediction of precipitation impacts due to the warming process. As we will see, this constraint is far more faithfully obeyed for mean precipitation than it is for the extremes which we find to be significantly underpredicted on the basis of surface temperature increase alone.

**Table 1.** Simulations of the Physics Ensemble and Their Selected Parameterization

Simulation	Microphysics	Cumulus Scheme	Land Model
<i>T</i>	WSM6	Kain-Fritsch	Noah LSM
<i>M</i>	Morrison	Kain-Fritsch	Noah LSM
<i>m</i>	-	-	Noah MP
<i>G</i>	Morrison	Grell-3	Noah LSM
<i>g</i>	-	-	Noah MP

## 2. Dynamical Downscaling Simulations

The regional climate model employed in our analyses is the Weather Research and Forecasting (WRF) model with the Advanced Research WRF (ARW) dynamic core [Skamarock *et al.*, 2008]. The simulations to be discussed herein have been performed using WRF version 3.4, with the following different configurations of the atmospheric physics parameterizations: the Rapid Radiative Transfer Model for Global coupled models (RRTMG) scheme for radiation of both short and long waves ([Iacono *et al.*, 2008] including the effect of variable trace gas concentrations); the Mellor-Yamada Nakanishi and Niino Level 2.5 scheme for planetary boundary layer parameterization [Nakanishi and Niino, 2009]; for microphysics, either the WRF Single-Moment 6-class (WSM6) [Hong and Lim, 2006] or the Morrison *et al.* [2009]'s scheme; and for Cumulus parameterization, either a modified version of the Kain-Fritsch scheme [Kain, 2004] or the Grell-3 scheme mostly based on the Grell-Devenyi methodology [Grell and Dévényi, 2002] but allowing subsidence effects to be spread to neighboring grid columns. The land processes are represented by either the Noah land surface model (LSM) [Chen and Dudhia, 2001] or the Noah LSM with multiparameterization (MP) options [Niu *et al.*, 2011]. The specific five different mixtures of physics parameterizations employed to define the different members of the physics ensemble are summarized in Table 1: configuration *T* can be compared to *M* for the effect of the microphysics scheme; *M* and *m* can be compared to *G* and *g*, respectively, for the effect of the cumulus scheme; whereas *M* and *G* can be compared to *m* and *g* to investigate the impact of the choice of land surface model.

These five different physics configurations have been employed to dynamically downscale an original Community Earth System Model 1 (CESM1) simulation, composed of an historical period driven by a combination of anthropogenic and natural forcing (1850–2005) and a future period following the Representative Concentration Pathways 8.5 (RCP8.5) scenario (2006–2100). This simulation was run at the default nominal 1° resolution whose performance for historical and future periods has been extensively described, notably in Gent *et al.* [2011] and Meehl *et al.* [2012]. One historical ensemble and one future ensemble of WRF simulations (Table 1) are forced by 6-hourly output from the CESM1 simulation during two distinct 15 year periods, 1979–1994 and 2045–2060, respectively.

The downscaling follows the same two-step nesting procedure employed in Gula and Peltier [2012], in which the first nested outer domain is of North American continental scale at 30 km resolution, whereas the innermost domain at 10 km resolution covers the Great Lakes Basin and extends into the northern portion of the Canadian province of Ontario. Compared to Gula and Peltier [2012], the local domain of interest (i.e., the inner domain) is identical, whereas the outer domain has been slightly extended to the South in order to include the entire Gulf of Mexico which was found to significantly improve the representation of summer precipitation over the continent. Furthermore, the lake model FLake [Mironov, 2008] that was employed offline by Gula and Peltier [2012] is now fully coupled to WRF in the simulations to be described in what follows.

## 3. Simulations of Historical Climate

To assess the quality of the representation of the mean climate within the inner domain, the seasonal and annual averages of the five historical simulations have been compared to the Climate Research Unit (CRU) time series historical data sets version 3.1 for the 2 m height surface air temperature [Harris *et al.*, 2013] and to a combination of two high-resolution precipitation data sets, CONUS version 1.2 over the CONtiguous United States [Livneh *et al.*, 2013] and the NRCan data set over Canada [Hutchinson *et al.*, 2009].

All simulations are characterized by a surplus of total precipitation on the order of 0.5 mm/d in spatial average, slightly smaller in winter and larger in summer, but with the largest spatial spread of the bias in summer (Figure 2). Simulations based upon the use of the Kain-Fritsch cumulus scheme (*T*, *M*, and *m*), in particular, have excess precipitation in the southeast corner of the domain (in the vicinity of lakes Ontario, Huron,

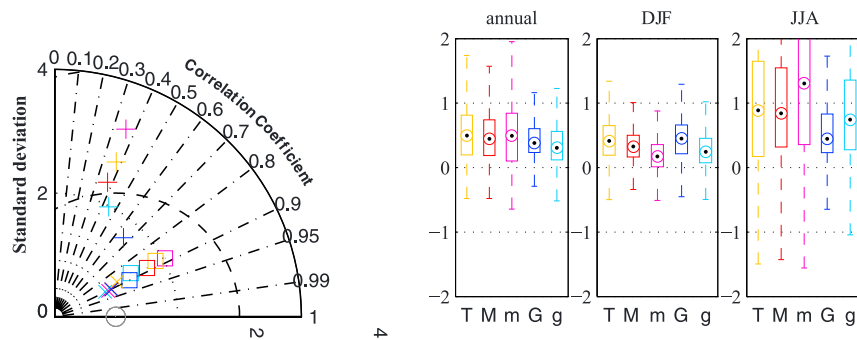


**Figure 2.** (left) Taylor diagram of annual (square), June-July-August (plus), and December-January-February (cross) averages of precipitation compared with the CONUS and NRCan data sets for the period 1979–1994 (see Figure 3). Each member of the WRF ensemble is represented by a different color. For all seasons to appear in the same diagram, observations and simulations have been normalized by the corresponding observation standard deviation. (right) Boxplots of the grid cell averaged precipitation differences between the simulations and the CONUS and NRCan data sets (in mm/d).

and Erie) in summer and too little precipitation near the Western boundary of the domain (west and northwest of lakes Michigan and Superior) in winter (Figures 2 and 3). The *G* simulation, with the Grell-3 cumulus scheme (Figure 1), can be considered the best simulation in terms of precipitation in all seasons despite a slightly larger precipitation deficit but a more spatially homogenous bias in all seasons (Figure 2).

In terms of temperature, all simulations provide a good representation of the spatial pattern of temperature with an annually averaged cold bias of 1 to 2°C (Figures 4 and 5). The performance in terms of summer temperature is the reverse of that for precipitation: in particular all simulations based upon use of the Grell-3 cumulus scheme (*G* and *g*) are characterized by a cold bias larger than 2°C in summer, whereas simulations with the Kain-Fritsch scheme have very little bias in summer. In winter, all simulations have a cold bias, with a tendency for simulations based upon use of the Noah MP land surface model (*m* and *g*) to be colder than their counterparts based upon use of the Noah LSM (*M* and *G*). Ultimately, the *M* simulation can be considered to deliver the most accurate results for temperature.

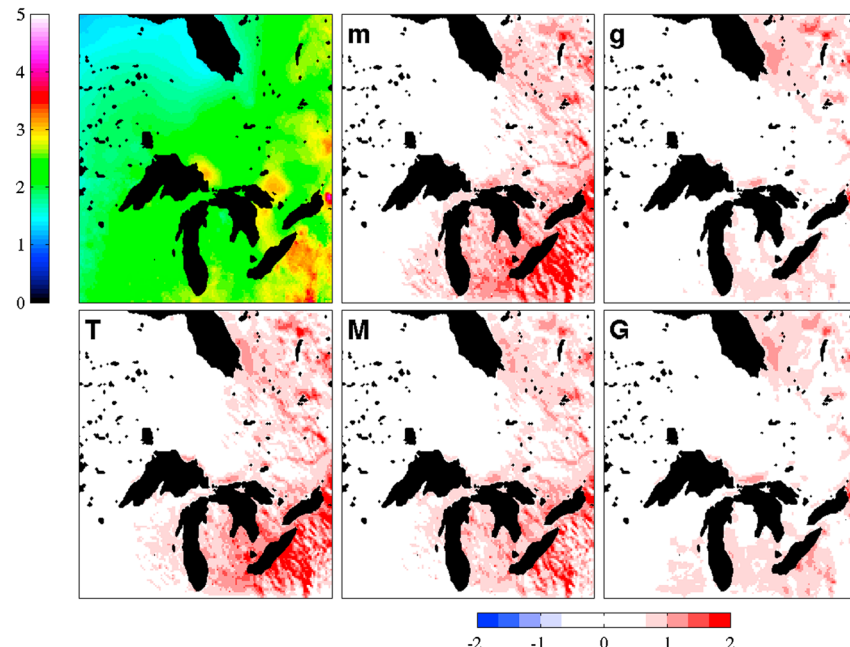


**Figure 3.** Annual average of precipitation from the 1979–1994 CONUS and NRCan data sets (top left) and annually averaged biases of the five simulations of which the WRF ensemble is comprised (in mm/d).

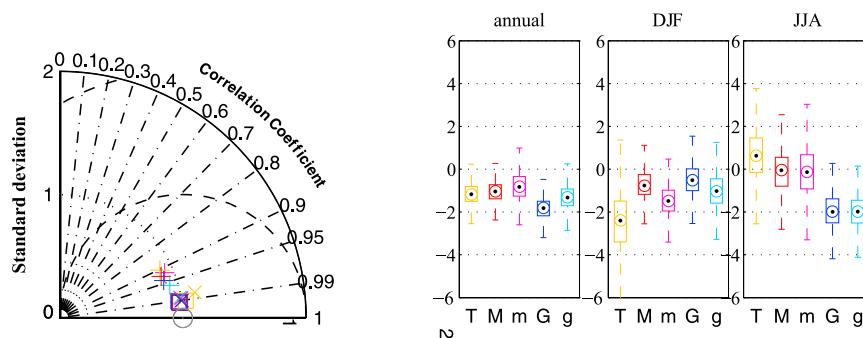


**Figure 4.** Same as Figure 2 but for temperature with observations from the CRU data set (in K).

#### 4. Historical Simulation of Daily Precipitation Extremes

To assess the quality of the representation of extreme precipitation events in the historical simulations, long observational time series are needed. Both the gridded NRCan and CONUS precipitation data sets provide daily precipitation and could have been employed for this purpose. However, as noted by Hutchinson *et al.* [2009], “the percentage errors in daily precipitation and daily precipitation extremes are relatively large (due to the) inevitable consequence of the high spatial complexity associated with daily precipitation that is below the spatial resolution of most data networks.” So instead of employing the gridded data sets, we decided to compare the precipitation extremes obtained in our simulation directly to the extremes obtained from weather station daily precipitation time series, from which the CONUS and NRCan gridded data sets were in large part derived. To this end, the daily total precipitations in the target region derived from the two following weather station data sets have been employed: namely, the Canadian Adjusted Precipitation Data Set (CAPD) [Mekis and Vincent, 2011] and the U.S. Historical Climatology Network data set (USHCN) [Menne *et al.*, 2012]. Although this approach ultimately requires that we compare point source observed time series directly with gridded simulated time series, a comparison which can be problematic, the good simulation-observation match described further below for the amplitude of 50 year extreme precipitation events will be construed *a posteriori* as a validation of this approach.

The CAPD time series have been corrected for numerous known measurements issues in order to perform trend analysis [Mekis and Vincent, 2011]. The USHCN time series have internal quality control tests reported

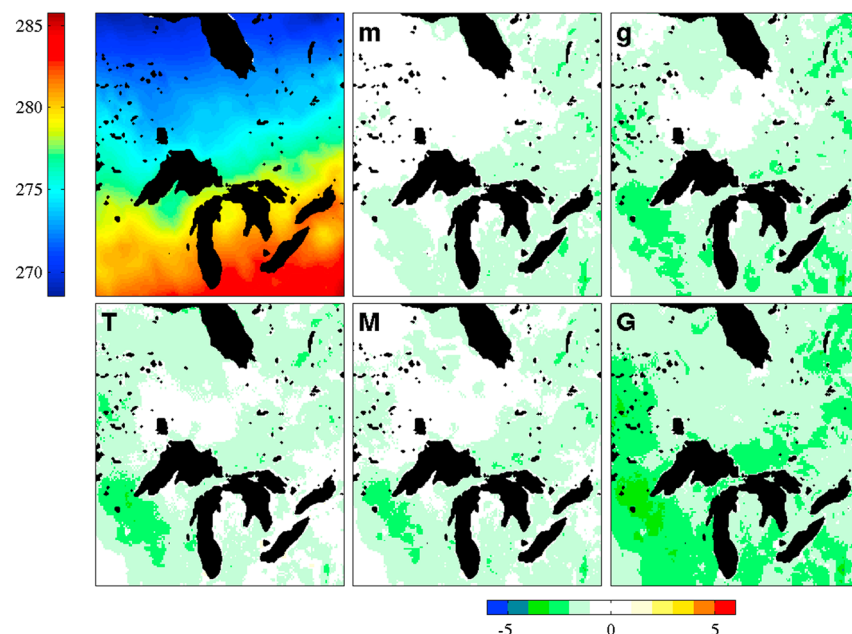


**Figure 5.** Same as Figure 3 but for temperature with observations from the CRU data set (in K).

and all values with a failed quality control flag have not been employed in our analysis. Neither data set is free of bias derivative of other issues (e.g., potential observer biases [Daly *et al.*, 2007]), which could influence the extreme value analysis performed for each individual station. However, because the aim in using these data sets is to validate the representation of extremes in the historical simulations globally, no further attempt has been made to correct each individual time series. Instead, we rely on the use of the largest number of stations with the longest time series possible in order to diminish the role of measurement issues in the overall validation process. The total number of Canadian and U.S. stations employed in this study (55 and 138, respectively) follows therefore from the selection of stations located inside the inner domain that include at least 50 accepted years (at each location, a single year of observations in either data set is accepted only if at least 75% of daily values are deemed valid). Ultimately, although each individual extreme value analysis employed in this study is potentially biased, the overall consistency of the observed extreme pattern between neighboring stations gives confidence *a posteriori* in the validation process we have employed.

#### 4.1. Extreme Value Analysis

The return values of daily precipitation extremes, for observed or simulated precipitation time series, are determined from a Generalized Pareto (GP) distribution which is fitted by the method of maximum likelihood to the tail of the distribution of each analyzed daily precipitation time series [e.g., Coles, 2001]. In the following, our focus will be upon the 50 year return value ( $X^{50}$ ) which has been chosen as a compromise between the duration of available observed daily precipitation time series, the rareness of the event of interest, and the uncertainty in the estimated return values based upon 15 year long simulations (This uncertainty is discussed further below.) In order to independently select the threshold parameter of each GP distribution, the tail is defined as comprising the 2.7 percentile largest values found in each full length record. This choice ensures a consistent threshold for time series of different duration (on the basis of which to compare observations and simulations), a consistent definition of heavy precipitation intensity  $I^H$  (to be defined in what follows), and also ensures that the GP distributions of historical and future simulations are based on the same number of daily values.

The procedure employed to compute  $X^{50}$  creates a very large spatial variability artifact in the simulations (Figure 1) due to the combination of the small spatial scale of extreme rain events and of the inherently large uncertainty in each  $X^{50}$  value when computed from one time series of only 15 year duration. Because of this spatial uncertainty, no attempts will be made to present results for any specific location. Instead, the focus will be on the overall comparison within the entire region, either at the 193 available station locations employed for the validation process (see below) or at all  $160 \times 160$  grid cells of the inner domain for future changes (next section).

Three modifications to the procedure described above have also been tested in order to examine the robustness of the  $X^{50}$  results presented in the following. First, instead of choosing the 2.7 percentile largest values of the entire time series (i.e., corresponding to an average of 10 daily values per year), we have also tested the results when choosing the 1.4 or 0.4 percentile largest values (average of 5 or 2 daily values per year, respectively). Second, instead of employing the GP distribution, the generalized extreme value (GEV) distribution has also been tested [e.g., Coles, 2001]. However, for the GEV case, a block approach has to be employed and the 10 largest values of each year of the time series have been selected to create the distribution to which the GEV was fitted by the method of maximum likelihood. Using multiple largest values per block for the GEV distribution is unusual, but it has been successfully applied in the past to increase the size of the distribution to be fitted by the GEV [e.g., Zhang *et al.*, 2004]. Third, instead of a 50 year period, the return values for 5, 10, or 20 year periods have also been analyzed. In the end, as long as the same method was used consistently for all observations and simulations, any combination of the three methodologies has delivered qualitatively similar results for extremes, both in terms of the observation-simulation comparison (presented below) or on the simulated historical-to-future changes (following sections). The validation and future changes described in the following are therefore considered robust.

#### 4.2. Validation of the Analysis of Extremes

The observation stations located in the inner simulation domain can be divided into three regions with different amplitudes of observed  $X^{50}$  values (Figure 1, bottom left): North of the Great Lakes  $X^{50}$  values are low in the 50–75 mm/d range; however, they are relatively high with 100 mm/d values east and south of lakes Huron, Erie, and Ontario; finally, they reach very large values, from 100 mm/d to 150 mm/d, south and west

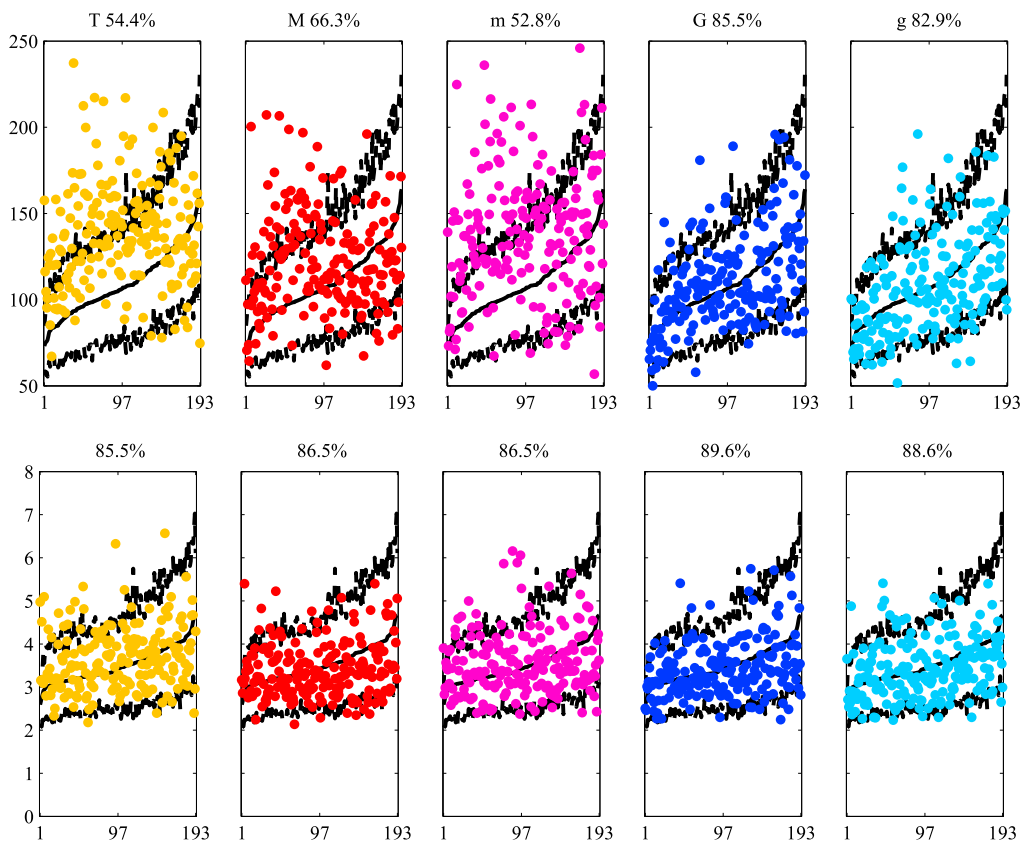


**Figure 6.** (top) In all panels,  $X_{\text{sta}}^{50}$  (in mm/d) of all weather stations computed from the complete historical record (black solid line) and the corresponding 90% confidence interval computed from 15 years subsamples (black dashed lines) are plotted as a function of the station numbers (stations are sorted from the smallest to the largest value for ease of visualization). The  $X^{50}$  value of the closest grid cell of each station is plotted in a different color for each configuration ( $T$ - $M$ - $m$ - $G$ - $g$  from left to right). The percentage of stations with simulated values inside the observational confidence interval is indicated above each diagram. (bottom) Same as Figure 6 (top) except for the recalibrated observed and simulated values  $X_{\text{sta}}^{50}/I^H_{\text{sta}}$  and  $X^{50}/I^H$ .

of lakes Michigan and Superior, with the largest  $X^{50}$  values at the southernmost locations. It is important to note that this spatial pattern of  $X^{50}$  amplitudes does not correspond to the observed pattern of mean precipitation: the annually averaged precipitation maximum is located in the southeast corner of the domain (Figure 3), and the summer precipitation is equally large in the two southern corners of the domain as well as the northeast corner (not shown). This highlights the fact that spatial locations of the extremes are not related in a straightforward manner to spatial variations of mean precipitation.

Because the simulations have a fixed 15 year duration, whereas each observation record has a variable duration of 50 years or more, a confidence interval is specifically computed for each weather station from a distribution of the  $X^{50}$  values obtained when only 15 years of observation were used. This  $X^{50}$  distribution is obtained from a subsampling bootstrap procedure where 1000 combinations of 15 years of the original time series are randomly selected and each combination is employed to compute  $X^{50}$  as described above. In essence, an  $X^{50}$  value obtained in the simulations will be said to well represent the observed  $X^{50}$  value at the 90% confidence level if it falls into the 5–95% interval of the subsampling bootstrap distribution.

When the  $X_{\text{sta}}^{50}$  values for each weather station are directly compared to the  $X^{50}$  value of the grid cell closest to the station location (Figure 6, top row), it is readily apparent that the Grell-3 simulations perform better in representing precipitation extremes in our domain, with the  $G$  simulation having more than 85% of the station  $X^{50}$  values well represented by that from the closest grid cell. Among the five configurations, the two simulations with the Grell-3 cumulus scheme ( $G$  and  $g$ ) seem to well represent this three region patterns in  $X^{50}$  amplitude (Figure 7). These are the same simulations that provide the best match to the observed mean precipitation field (Figure 1).

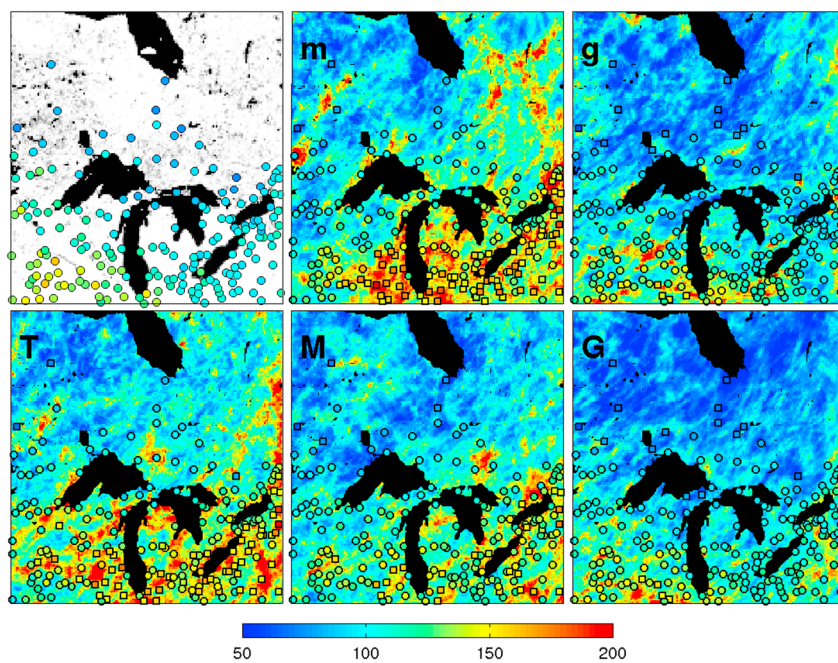


**Figure 7.**  $X_{\text{sta}}^{50}$  (in mm/d) from all U.S. and Canadian weather stations with an historical record of at least 50 years (top left). The other panels display  $X^{50}$  for all five simulations with the recalibrated-value  $X_{\text{sta}}^{50}(I^H/I_{\text{sta}}^H)$  of all weather stations overlaid. Weather station values are plotted as a circle (square) if the recalibrated value  $X_{\text{sta}}^{50}(I_{\text{sta}}^H/I^H)$  is (not) inside the observational confidence interval (see text and Figure 6 from the main manuscript for details).

The configurations with the Kain-Fritsch cumulus scheme (*T*, *M*, and *m*) display  $X^{50}$  values that are excessive (Figure 6, top row), mostly in the eastern and southeastern parts of the domain (Figure 7), but a straightforward recalibration of  $X^{50}$  by the heavy precipitation intensity ( $I^H$ ) gives a statistical match with observations larger than 85% for all simulations (Figure 6, bottom row). By heavy precipitation intensity,  $I^H$  refers to the average of the 2.7 percentile of the largest daily precipitation amounts. Note that when the recalibrated  $*X_{\text{sta}}^{50}$  values from each station ( $*X_{\text{sta}}^{50} = X_{\text{sta}}^{50}(I^H/I_{\text{sta}}^H)$  where  $I^H$  is taken from the closest simulation grid point in the domain) is plotted over the  $X^{50}$  field of each simulation, station recalibrated values are virtually indistinguishable from the spatial variability of each simulation (Figure 7).

Using the yearly average precipitation or the mean precipitation intensity (i.e., the mean of all wet days) instead of  $I^H$  for the recalibration of  $X_{\text{sta}}^{50}$  would not have improved the result, but rather degraded the observation-simulation match because the mean and extreme values are not proportionally related between the different regions of the domain. Most importantly, because the computation of  $X^{50}$  and  $I^H$  are both based on the highest 2.7 percentile values of the precipitation distribution, the good observation-simulation match for all simulations after recalibration is an indication that the shape parameters of the Pareto distribution found for the observations and the simulations tend also to be similar, in other words that the observations and the simulations have tail distributions of the same degree of “heaviness.”

Although the configurations with the Kain-Fritsch cumulus scheme (*T*, *M*, and *m*) display  $X^{50}$  values that are excessive (Figure 6, top row), they are nevertheless employed in the next section to assess the future change in mean and extreme precipitation for two main reasons: first, the next section deals with the relative future changes in precipitation that can be assumed to be independent of the original bias (corrected by the straightforward recalibration described previously) and second, the next section focuses upon the relationship between precipitation change and temperature change and these configurations (particularly configuration *M*) have been shown to better represent temperature.

## 5. Projections of Future Daily Precipitation

After having provided evidence that the simulations of the physics ensemble compare well to past observations, this section presents the changes in mean and extreme precipitation projected to be characteristic of future conditions (2045–2060) relative to the historical simulations (1979–1994). Everywhere in the Great

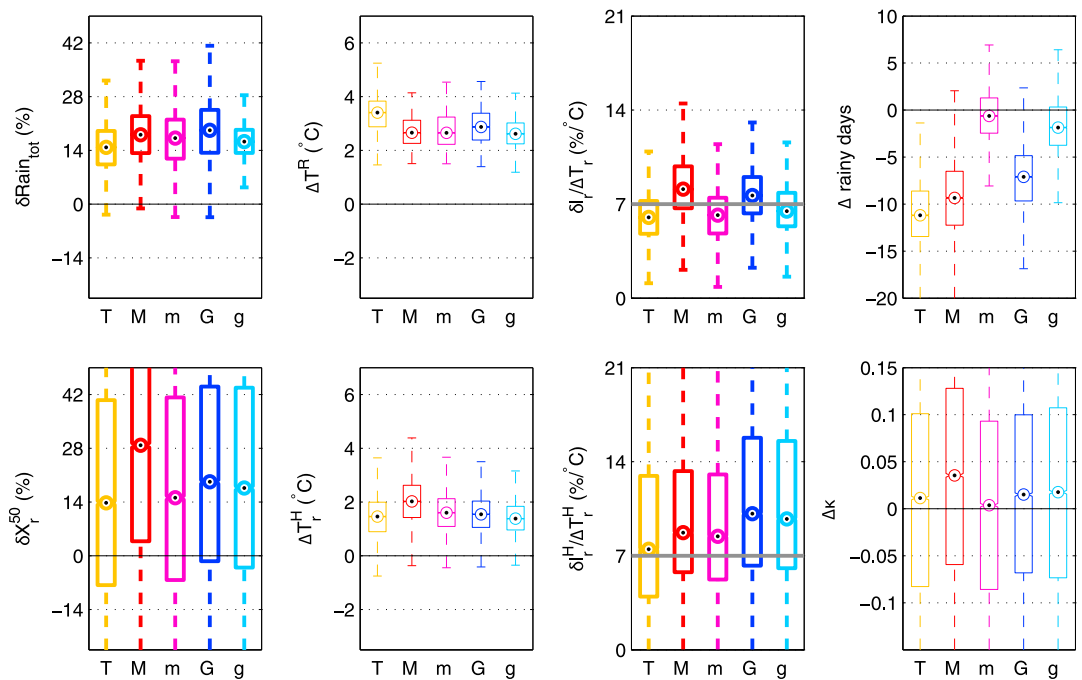


**Figure 8.** Boxplots of the distribution over all grid cell points of future changes. Each box corresponds to one configuration (same color as Figure 6). Median changes are highlighted with black dots. (top row) Change in yearly average rainfall ( $\delta\text{Rain}_{\text{tot}}$ ), in surface temperature of the average rainy day composite ( $\Delta T_r$ ), in rainfall of the average rainy day composite normalized by the surface temperature change ( $\delta l_r/\Delta T_r$ ), and in number of rainy days per year ( $\Delta$  rainy days). (bottom row) Change in  $X_r^{50}$ , in surface temperature of the heavy rainfall composite ( $\Delta T_r^H$ ), in rainfall of the heavy rainfall composite normalized by the surface temperature change ( $\delta l_r^H/\Delta T_r^H$ ), and in the shape parameter ( $\Delta\kappa$ ) of the GP distributions used to compute  $X_r^{50}$ . Notations  $\delta$  and  $\Delta$  correspond to relative changes (in percent) and absolute changes (unit in the ordinate label), respectively.

Lakes region, the most extreme of the 2.7% largest daily precipitation events employed previously to compute  $X_r^{50}$  are rainfall events. As such, the following discussion will focus on changes in liquid precipitation, both average and extremes. Also, because of the large uncertainty in single  $X_r^{50}$  values discussed earlier, no attempt will be made to present changes for specific geographical locations. Instead, the distribution of changes over all grid cells are presented for each configuration in Figures 8–10, and the following discussion will focus on the median changes.

All configurations show an unequivocal increase in rainfall by midcentury, both in averages and extremes (Figure 8, first column,  $\delta\text{Rain}_{\text{tot}}$  and  $\delta X_r^{50}$ ). Both extreme and mean increases have a median increase larger than 13% in all configurations, and as will be shown in the following, a large part (if not all) can be explained by the increased temperature and the associated thermodynamically predicted increase of atmospheric moisture content. For each grid cell, a composite of a heavy rainfall event is created by averaging the atmospheric characteristics (rainfall, temperature, water vapor mixing ratio...) of the 2.7% largest daily rain events of each simulation. Composites of an average rainy day are also created to analyze the average changes in liquid precipitation.

### 5.1. Total Rainfall Changes

The surface temperature changes of the average rainy day composites have a distribution similar for all model configurations, with a median increase close to  $2.7^\circ\text{C}$ , with the exception of configuration  $T$  for which the increase is  $3.4^\circ\text{C}$  (Figure 8,  $\Delta T_r$ ). But most importantly, inspection of the relative increase in average rain intensity (i.e., rainfall of the average composite,  $\delta l_r$ , sometimes called the simple daily intensity index) demonstrates that all configurations have a median value very close to the optimum Clausius-Clapeyron value of 7% per  $^\circ\text{C}$  of warming (Figure 8,  $\delta l_r/\Delta T_r$ ). The median increase of the surface water vapor mixing ratio of the composite is, in fact, even closer to the optimum 7% per  $^\circ\text{C}$  for all configurations (Figure 10).

It is important to note that the use of the rainy day composites to determine the temperature and rain intensity changes is critical to obtaining this good match to the Clausius-Clapeyron prediction, whereas the

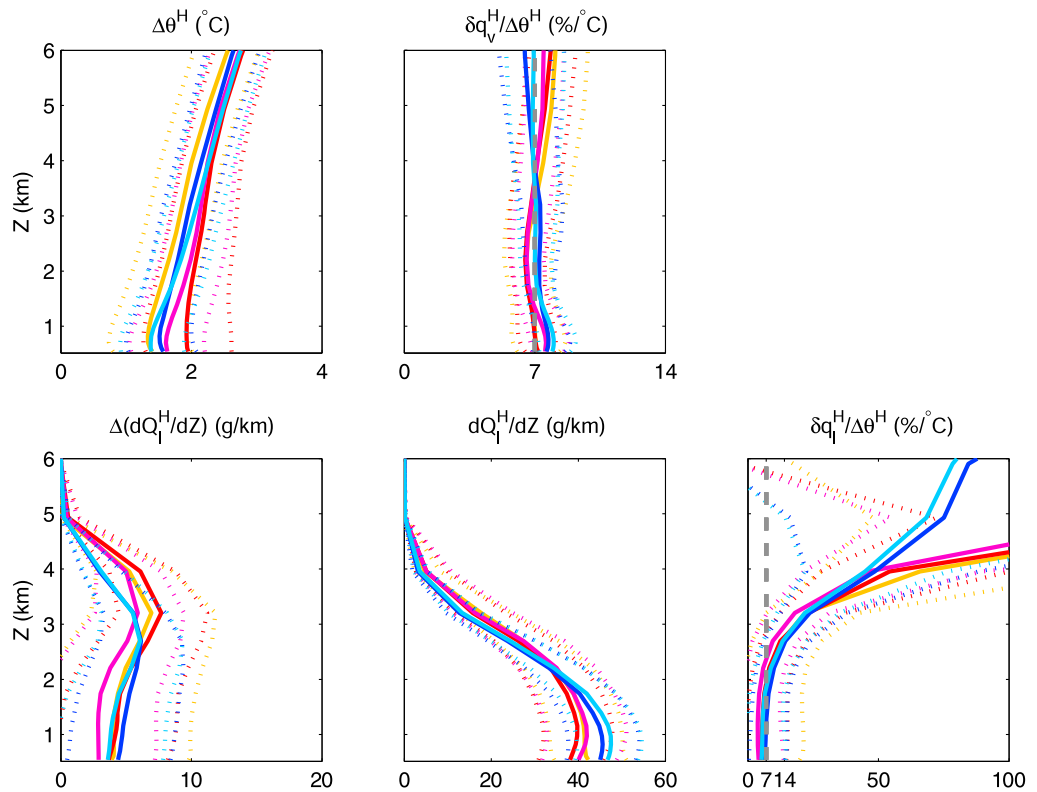


**Figure 9.** Median (solid line) and first and third quartiles (dotted line) of the distribution of the vertical profiles of the heavy rainfall composites function of the unipotential height ( $Z$  in km). Each configuration is plotted with a different color (same as in Figure 6). (top row) Future changes in potential temperature ( $\Delta\theta^H$ ) and sensitivity of future changes in water vapor mixing ratio to potential temperature ( $\delta q_v^H/\Delta\theta^H$ ). (bottom row) Future changes (left) and initial state (center) of liquid water mass ( $Q_l^H$ ) as a proxy of rain production and sensitivity of future changes in liquid water mixing ratio to potential temperature ( $\delta q_l^H/\Delta\theta^H$ ) (right).

changes in rainfall and temperature averaged over a given period (e.g., year and summer) would usually show a smaller increase than 7% per °C: this difference can arise either because of the larger temperature changes reported when averaged over every day instead of over rainy days only or because of the changes in the number of rainy days during a given period, as, for instance, the decrease in the number of rainy days in our future simulations (Figure 8,  $\Delta$  rainy days).

Overall, when comparing all physics configurations, the future changes in rainfall intensity follow the Clausius-Clapeyron prediction quite closely and are therefore mostly due to thermodynamic changes. There is, however, the possibility of a small modulation in our physics ensemble related to the choice of land model: both configurations *M* and *G* that employ the Noah LSM tend to show a larger sensitivity of rain intensity to surface temperature changes as well as a larger decrease in the number of rainy days than their configuration counterparts *m* and *g* with Noah MP (Figure 8). This influence of the choice of land model on the projection of future average rain changes will need to be further tested in a larger ensemble of downscaled results.

### 5.2. Heavy Rainfall Changes

The 50 year return period of daily precipitation amount is found to have a median increase in amplitude of 14% to 29% by midcentury depending on the configuration (Figure 8,  $X_r^{50}$ ). Because these relatively rare events are not explicitly represented for all grid cells in a 15 year simulation, the changes in the heavy rainfall composites based on the 2.7% largest rainy days will be discussed in this subsection before being employed in the next subsection as a proxy that will assist us in understanding the cause of such a large increase in very extreme events.

The analysis of the heavy rainfall composites of each simulation reveals a similar explanation for the future changes in heavy rainfall events as that found with the average composite for total rainfall changes: most

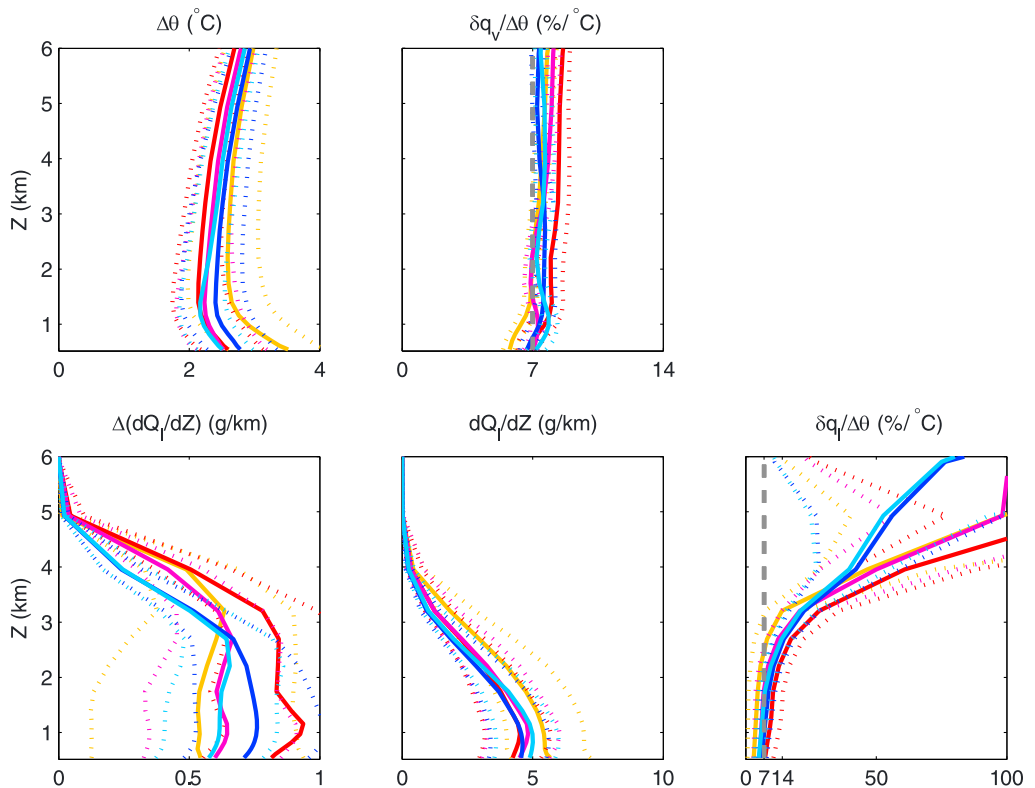


**Figure 10.** Same as Figure 9 except for the average composites of a rainy day instead of the heavy rainfall composites.

of the changes in heavy rainfall can also be attributed to the thermodynamic effect since the sensitivity of heavy rainfall intensity to surface temperature changes is at, or above, the 7% per °C of warming that the thermodynamic Clausius-Clapeyron relation would predict for the increase in atmospheric moisture (Figure 8,  $\delta I_r^H/\Delta T_r^H$ ). The values larger than the 7% reference from thermodynamics can be explained on the basis of two changes in the vertical structure of the rain events.

First, because a significant portion of rain originates from the midtroposphere and, because midtropospheric warming in the inner domain is larger than surface warming in summer when most heavy rainfall occurs (Figure 9,  $\Delta\theta$ ), there is therefore an artifact that appears as a consequence of employing local surface temperatures to assess the predictive capacity of the Clausius-Clapeyron relation for heavy precipitation changes. In fact, the vertical structure of moisture changes in the heavy rainfall composite follows almost exactly the Clausius-Clapeyron relation in the troposphere when using the vertical profile of potential temperature changes instead of the surface temperature alone (Figure 9,  $\delta q_v/\Delta\theta$ ).

Second, it follows from inspection of the vertical profile of the rain changes that the heavy rainfall composites display a clear maximum between 2500 and 3500 m of altitude near the midtroposphere and above the vertical maximum of rain production located below 2000 m (Figure 9,  $\Delta(dQ_r/dZ)$  and  $dQ_r/dZ$ ). This vertical maximum in the change of the rain structure of the heavy rainfall composite contrasts with the change in the average composite which is fairly uniform with height (Figure 10). In fact, this maximum located at the top of the rain structure demonstrates that the heavy rainfall events will tend to produce rain at a slightly higher altitude in the future. Because there is significant moisture in the midtroposphere but very little rain is produced there, by extending to higher altitude, future heavy rainfall events will be able to produce even more rain.

Although the thermodynamic Clausius-Clapeyron relation should technically be applied only for the analysis of water vapor mixing ratio, it is interesting to note that the future change in liquid water mixing ratio also follows the 7% per °C of warming quite well, but only up to approximately 2500 m in altitude (Figure 9,  $\delta q_r/\Delta\theta$ ). It seems therefore clear that the increase of rain production above 2500 m is primarily the result of future production of rain at altitudes where very little rain was produced in historical simulations. Because

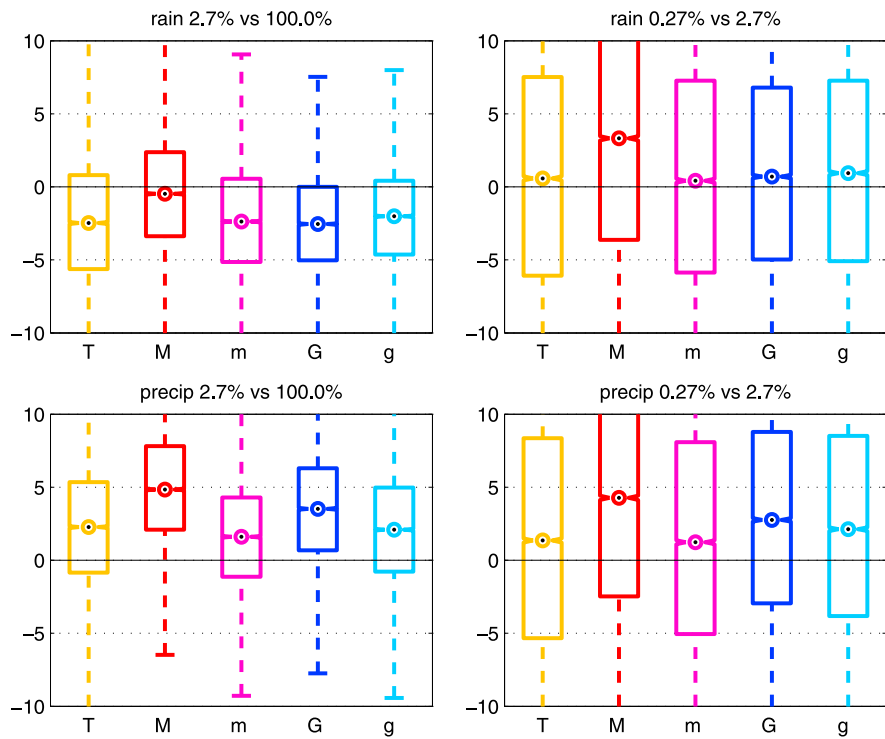


**Figure 11.** (top row) Boxplots of the future changes in the relative importance (in percent) of (left) the contribution of the tail of the rainfall distribution to the total amount of rainfall and (right) the contribution of the extremes to the cumulative rainfall amount from the tail alone. The tail is defined as the 2.7% largest daily rainfall amounts while the extremes of the tails are defined as the 10% largest values of the tail (or equivalently as the 0.27% largest daily rainfall amounts). Each box corresponds to one configuration as in Figure 8. (bottom row) Same as Figure 11 (top row) but for the total precipitation instead of the rainfall only.

the future change in liquid water mass above 2500 m corresponds to between 36 and 48% of the total change, this confirms that a significant portion of the increase is due to heavy rainfall events reaching higher altitude and not only to a purely thermodynamic effect.

### 5.3. Changes in Rainfall Distribution

The two effects discussed above for the heavy rainfall composite, i.e., larger midtropospheric warming and rain production at higher altitudes, are likely to further exacerbate very large extreme and rare rainfall events, such as those represented by  $X_r^{50}$ , which are expected to reach the highest altitude. Thermodynamical effects related to temperature increase will therefore be the primary factor responsible for determining the increase in extreme rainfall amount, but such effects in the vertical structure of rain production are good candidates for explaining the projected fatter tail of the rainfall distribution as seen from the increase of the shape parameters of the fitted Pareto distributions (Figure 8,  $\Delta\kappa$ ).

It is important to note that, on the one hand, the contribution of the entire tail of the rainfall distribution to the total amount of rain (median values for all configurations between 36 and 41%) is decreasing in the future and, on the other hand, the contributions of the extremes to the rainfall amount of the entire tail (median values of between 19 and 21%) is increasing in the future (Figure 11, top). These two facts explain why the extremes (and the 50 year extreme rainfall events among them) can display a similar increase as for the total amount of rainfall (Figure 8 (left)  $\delta\text{Rain}_{\text{tot}}$  and  $\delta X_r^{50}$ ) despite the projected fatter tail of the rainfall distributions. The increase of the shape parameters of the fitted Pareto distributions (Figure 8,  $\Delta\kappa$ ) derives in fact directly from the increased contribution of the extremes to the overall rainfall amount of the tail.

In summary, the median future change in rainfall distribution in the region of the Great Lakes corresponds to a global increase of total precipitation but with a larger contribution of low and extreme rainy days and a smaller contribution from the medium and heavy rainy days. This change is compatible with both a future reduction in the number of rainy days and a fatter tail of the daily rainfall distribution (Figure 8 (right),  $\Delta$  rainy days and  $\Delta\kappa$ ).

Finally, considering the total precipitation distributions, it will be clear that there is an increase of the contributions of both the heavy precipitation to the total precipitation and of the extreme precipitation to that in the entire tail of the distribution (Figure 11, bottom). This is in contrast to the result just described for the rainfall distributions, but this also highlights the fact that a portion of the changes in the rainfall distributions is also due to snowfall changes which are significant in the Great Lakes region. Not only are the rainfall distributions changing because extreme rainfall events are changing during the warmer warm season but also because of a reduction in snowfall during the warmer cold season and a concomitant increase in low rainfall.

## 6. Summary and Discussion

The historical simulations based upon the physics ensemble presented herein provide a good representation of average and extreme precipitation over the Great Lakes Basin and the Canadian province of Ontario. However, as is often the case with ensembles based upon regional climate model simulations, no particular simulation can be thought to best represent both precipitation and temperature. Nevertheless, and despite different observational biases in precipitation and temperature, the physics ensemble presented herein provides a very coherent projection of the future moisture availability increases due to the temperature increase (predicted on the basis of the Clausius-Clapeyron relation) which directly drives the rainfall increase both in average and extremes. Details of the physics parameterization (precipitation and land model) appear to play only a secondary role in determining the future changes, mostly through their impact on future temperature changes.

In the dynamically downscaled simulations detailed here, the value of 7% increase per °C of warming seems to be an even better predictor of precipitation changes over the Great Lakes basin than might have been expected on the basis of previous analyses based on global model simulations [e.g., Tebaldi *et al.*, 2006; Pall *et al.*, 2007; Kharin *et al.*, 2007, 2013]. However, because the downscaling ensemble has been forced in our analyses by a unique global simulation, further ensembles designed to more fully capture the variability associated with initial conditions from the global parent model will need to be employed to confirm the robustness of this result.

All of the existing simulations are also characterized by a fattening of the tail of the daily precipitation distribution, in the sense that the contribution of the extremes to the overall rainfall amount of the tail of the distribution is projected to increase in the future. The largest median increase of the "once in 50 year rainfall event" is 29% by midcentury, which is 11% more than the projected average increase (configuration M, Figure 8). Such a large-amplitude increase can also be reexpressed in terms of an increase in the frequency of events of a fixed amplitude, such that current 50 year extreme events could happen as often as every 25 years by midcentury. The fattening of the tail of the precipitation distribution is usually described as being driven either by thermodynamical and/or future circulation changes [e.g., Meehl *et al.*, 2005; Pall *et al.*, 2007]. Although this increase corresponds to an increase larger than the thermodynamical constraint of 7% per °C of warming, the mechanism suggested on the basis of our simulations does not seem to involve any large-scale circulation changes but only to involve extreme events producing rain at a higher altitude. However, large-scale circulation changes cannot be entirely ruled out at this point, as they might play a role in explaining the larger warming at midtroposphere than at the surface during the summer season when large rain events usually occur in the Great Lakes region.

## References

- Alexander, L., et al. (2006), Global observed changes in daily climate extremes of temperature and precipitation, *J. Geophys. Res.*, 111(D5), D05109, doi:10.1029/2005JD006290.
- Chen, F., and J. Dudhia (2001), Coupling an advanced land surface-hydrology model with the Penn State-NCAR MM5 modeling system. Part I: Model implementation and sensitivity, *Mon. Weather Rev.*, 129(4), 569–585.
- Coles, S. (2001), *An Introduction to Statistical Modeling of Extreme Values*, 209 pp., Springer, London, U. K.
- Daly, C., W. P. Gibson, G. H. Taylor, M. K. Doggett, and J. I. Smith (2007), Observer bias in daily precipitation measurements at United States cooperative network stations, *Bull. Am. Meteorol. Soc.*, 88, 899–912.
- Di Luca, A., R. de Elía, and R. Laprise (2013), Potential for small scale added value of RCMs downscaled climate change signal, *Clim. Dyn.*, 40(3–4), 601–618.
- Gent, P. R., et al. (2011), The community climate system model version 4, *J. Clim.*, 24(19), 4973–4991.
- Grell, G. A., and D. Dévényi (2002), A generalized approach to parameterizing convection combining ensemble and data assimilation techniques, *Geophys. Res. Lett.*, 29(14), 38.1–38.4, doi:10.1029/2002GL015311.
- Gula, J., and W. R. Peltier (2012), Dynamical downscaling over the Great Lakes basin of North America using the WRF regional climate model: The impact of the Great Lakes system on regional greenhouse warming, *J. Clim.*, 25(21), 7723–7742.

## Acknowledgments

The simulations discussed in this paper were performed in part on the SciNet High Performance Computing facility of the University of Toronto which is a component of the Compute Canada HPC platform. Analyses also made significant use of the SOSCIPI Blue Gene/Q system that is also operated by SciNet. M.D.O. was supported by a SOSCIPI Post-doctoral Fellowship, and ARE was partially supported by a SOSCIPI Graduate Student Fellowship; the research of WRP is supported by NSERC Discovery grant A9627. The authors would like to thank Éva Mekis for providing the Canadian Adjusted Precipitation data set and Dan McKenney for providing the NRCan high-resolution precipitation data set. The CRU-TS Version 3.10, the CONUS Version 1.2, and the US-GHCN Version 3.11 observational data sets employed in this study are publicly available online at <http://www.cru.uea.ac.uk/cru/data/hrg/>, <ftp://ftp.hydro.washington.edu/pub/blivneh/CONUS/>, and <http://www.ncdc.noaa.gov/cdo-web/>, respectively.

- Harris, I., P. Jones, T. Osborn, and D. Lister (2013), Updated high-resolution grids of monthly climatic observations—The CRU TS3.10 dataset, *Int. J. Climatol.*, 34, 623–642.
- Hong, S.-Y., and J.-O. J. Lim (2006), The WRF single-moment 6-class microphysics scheme (WSM6), *J. Korean Meteor. Soc.*, 42(2), 129–151.
- Hutchinson, M. F., D. W. McKenney, K. Lawrence, J. H. Pedlar, R. F. Hopkinson, E. Milewska, and P. Papadopol (2009), Development and testing of Canada-wide interpolated spatial models of daily minimum/ maximum temperature and precipitation 1961–2003, *J. Appl. Meteorol. Climatol.*, 48, 725–741.
- Iacono, M. J., J. S. Delamere, E. J. Mlawer, M. W. Shephard, S. A. Clough, and W. D. Collins (2008), Radiative forcing by long-lived greenhouse gases: Calculations with the AER radiative transfer models, *J. Geophys. Res.*, 113(D13), D13103, doi:10.1029/2008JD009944.
- Kain, J. S. (2004), The Kain–Fritsch convective parameterization: An update, *J. Appl. Meteorol.*, 43(1), 170–181.
- Kharin, V. V., F. W. Zwiers, X. Zhang, and G. C. Hegerl (2007), Changes in temperature and precipitation extremes in the IPCC ensemble of global coupled model simulations, *J. Clim.*, 20(8), 1419–1444.
- Kharin, V. V., F. W. Zwiers, X. Zhang, and M. Wehner (2013), Changes in temperature and precipitation extremes in the CMIP5 ensemble, *Clim. Change*, 119(2), 345–357.
- Livneh, B., E. A. Rosenberg, C. Lin, B. Nijssen, V. Mishra, K. M. Andreadis, E. P. Maurer, and D. P. Lettenmaier (2013), A long-term hydrologically based dataset of land surface fluxes and states for the conterminous United States: Update and extensions, *J. Clim.*, 26, 9384–9392.
- Meehl, G. A., J. M. Arblaster, and C. Tebaldi (2005), Understanding future patterns of increased precipitation intensity in climate model simulations, *Geophys. Res. Lett.*, 32(18), L18719, doi:10.1029/2005GL023680.
- Meehl, G. A., et al. (2012), Climate system response to external forcings and climate change projections in CCSM4, *J. Clim.*, 25(11), 3661–3683.
- Mekis, É., and L. A. Vincent (2011), An overview of the second generation adjusted daily precipitation dataset for trend analysis in Canada, *Atmos. Ocean*, 49(2), 163–177.
- Menne, M., I. Durre, R. Vose, B. Gleason, and T. Houston (2012), An overview of the global historical climatology network-daily database, *J. Atmos. Oceanic Technol.*, 29, 897–910.
- Mironov, D. (2008), Parameterization of lakes in numerical weather prediction. Description of a lake model, *COSMO Tech. Rep.* 11, Deutscher Wetterdienst, Offenbach am Main, Germany.
- Morrison, H., G. Thompson, and V. Tatarskii (2009), Impact of cloud microphysics on the development of trailing stratiform precipitation in a simulated squall line: Comparison of one-and two-moment schemes, *Mon. Weather Rev.*, 137(3), 991–1007.
- Nakanishi, M., and H. Niino (2009), Development of an improved turbulence closure model for the atmospheric boundary layer, *J. Meteorol. Soc. Jpn.*, 87(5), 895–912.
- Niu, G.-Y., et al. (2011), The community Noah land surface model with multiparameterization options (Noah-MP): 1. Model description and evaluation with local-scale measurements, *J. Geophys. Res.*, 116(D12), D12109, doi:10.1029/2010JD015139.
- Notaro, M., K. Holman, A. Zarrin, E. Fluck, S. Vavrus, and V. Bennington (2013), Influence of the Laurentian Great Lakes on regional climate, *J. Clim.*, 26(3), 789–804.
- Pall, P., M. Allen, and D. Stone (2007), Testing the Clausius–Clapeyron constraint on changes in extreme precipitation under CO<sub>2</sub> warming, *Clim. Dyn.*, 28(4), 351–363.
- Skamarock, W., J. Klemp, J. Dudhia, D. Gill, D. Barker, M. G. Duda, X.-Y. Huang, W. Wang, and J. G. Powers (2008), A description of the advanced research WRF version 3, *Tech. Note TN-475+STR*, NCAR, Boulder, Colo.
- Tebaldi, C., K. Hayhoe, J. M. Arblaster, and G. A. Meehl (2006), Going to the extremes, *Clim. Change*, 79(3–4), 185–211.
- Zhang, X., F. W. Zwiers, and G. Li (2004), Monte Carlo experiments on the detection of trends in extreme values, *J. Clim.*, 17(10), 1945–1952.